Subtractive NCE-MRA: Improved Background Suppression Using Robust Regression Based Weighted Subtraction

Authors:

Hao Li,[1*] Shuo Wang,[1,3] Martin J Graves, [1,2] David J Lomas[1], Andrew N Priest,[1,2]

[1]Department of Radiology, University of Cambridge, Cambridge, United Kingdom.

[2]Department of Radiology, Addenbrooke's Hospital, Cambridge, United Kingdom.

[3]Data Science Institute, Imperial College London, London, United Kingdom.

Correspondence

Hao Li

Department of Radiology

University of Cambridge

Box 218, Cambridge Biomedical Campus, Cambridge CB2 0QQ, United Kingdom.

Email: hl476@cam.ac.uk

Word count (body of text): 4846

Figure and table number: 10

Running head: Background Suppression for Subtractive NCE-MRA

ABSTRACT

Purpose:

To correct the intensity difference of static background signal between bright-blood images (BBIs) and dark-blood images (DBIs) in subtractive Non-contrast-enhanced MR Angiography (NCE-MRA) using robust regression, thereby improving static background signal suppression on subtracted angiograms.

Method:

Robust regression (RR), using iteratively reweighted least squares, is used to calculate the regression coefficient of background tissues from a scatter plot showing the voxel intensity of BBIs versus DBIs. The weighting function is based on either the Euclidean distance from the estimated regression line or the deviation angle. Results from RR using deviation angle (RRDA), conventional RR using the Euclidean distance (cRR) and ordinary least-squares regression (OLS) were compared with reference values determined manually by two observers. Performance was evaluated over studies using different sequences, including 36 thoracic Flow-Sensitive Dephasing (FSD) datasets, 13 iliac FSD datasets and 26 femoral Fresh Blood Imaging (FBI) datasets.

Result:

RRDA achieved robust and accurate performance in all types of images, with small bias, small mean absolute error and high correlation coefficients with reference values. Background tissues, such as muscle, veins and bladder, were suppressed while the vascular signal was preserved. cRR gave good performance for thoracic and iliac FSD but could not suppress background tissues in femoral FBI. OLS was sensitive to outliers and overestimated regression coefficients in thoracic FSD.

Conclusion:

Weighted subtraction using RR was able to acquire the regression coefficients of background signal and improve background suppression of subtractive NCE-MRA techniques. RRDA has the most robust and accurate overall performance among three regression methods.

Keywords:

non-contrast-enhanced; MR angiography; background suppression; robust regression

INTRODUCTION

Contrast-enhanced magnetic resonance angiography (CE-MRA) (1) is widely used for clinical evaluation of vascular anatomy and pathology (2,3) with the advantage of avoiding ionising radiation exposure. However, gadolinium-based contrast agents have raised concerns over their association with nephrogenic systemic fibrosis in patients with renal failure, and more recently over long-term deposition of gadolinium in the brain even in patients without severe renal dysfunction (4,5). Such concerns have stimulated the renaissance of non-contrast-enhanced (NCE) MRA techniques, which yield vascular images without injection of exogenous contrast agents (6,7).

Subtractive NCE-MRA is a class of techniques that acquires two image sets (dark-blood images (DBIs) and bright-blood images (BBIs)) with different vascular signal intensity (SI) which are later subtracted to generate angiograms. Typical subtractive NCE-MRA techniques include Flow-Sensitive Dephasing (FSD) (8–12) and Fresh Blood Imaging (FBI) (13,14). FSD dephases moving blood spins by applying specially designed flow-sensitive preparation schemes. Velocity-sensitised (DANTE (15,16) and iMSDE (8,17)) or acceleration-sensitised preparations (ADVANCE(10)) can be used to suppress either arterial signal or both arterial and venous signal. FBI uses a half-Fourier fast spin-echo pulse sequence to acquire data sets in systole and diastole. The arterial signal is suppressed during systole due to fast flow, which leads to dephasing of moving spins, while the signal is preserved in diastole due to slow flow.

In these conventional NCE-MRA techniques, the static background SIs from DBIs and BBIs should ideally be identical, leading to a complete absence of background signal in the subtracted images. However in practice, due to different imaging settings of the two acquisitions and the varying effective TR between the two acquisitions, some static background tissues show slightly different signal levels in BBIs and DBIs (9,18–24). For example, fat signal, if not sufficiently suppressed, can appear higher on BBIs for both FSD and FBI, leading to residual fat signal and stripe artefacts in the subtracted images (9,20,25). Muscle SI is normally higher on BBIs for FSD (18), but it could be slightly higher on DBIs for FBI (22,23). These residual background signals can potentially obscure the vascular signal of interest and affect clinical diagnosis. Venous contamination was also reported in FBI arteriogram (18,21,24), which can make angiographic interpretation challenging due to the close proximity of paired veins alongside peripheral arteries (6).

Residual background signals can potentially be suppressed by using a weighted subtraction. Weighted subtraction has been used in some MRA techniques, such as MRA using SSFP (26), HOP-MRA (27) and interleaved double-echo MR angiography and venography (28), to maximise the blood-to-background contrast. However, the weighting factor was selected manually and empirically. Our initial investigations demonstrated that the weighting factor for the subtraction in FBI and FSD can be obtained adaptively and automatically by performing a linear regression of the SIs (18,19). However,

simple linear regression methods, such as ordinary least-squares regression (OLS) and principal component analysis (PCA), can be affected by outliers from vascular tissues such as the heart and large arteries (18,19). Also, some background tissues with high SI on the DBI and BBIs are not given sufficient weighting in the regression procedure(s) to ensure that they are suppressed on the subtracted angiograms.

The purpose of this study is to develop robust regression methods to correct the SI difference of background tissues between the BBIs and DBIs and to improve the background suppression. Firstly, the signal levels of background tissues on BBIs and DBIs are evaluated in several different NCE-MRA techniques. Then, robust regression models, using iteratively reweighted least squares, are proposed to acquire the regression coefficient of the SI of background tissues on BBIs and DBIs—with the weighting function based on either the Euclidean distance or the deviation angle relative to the estimated regression line. Results from these two robust regression models, together with OLS, are compared with reference values subjectively determined by two observers over several different imaging sequences and in different vascular imaging areas.

THEORY

Characteristics of Residual Signal

Figure 1A is the scatter plot of the SI of each pixel on DBIs versus the SI on BBIs for one single slice (Figure 1B and 1C, 3D femoral artery FBI). Based on their anatomical location and intensity characteristics, all the pixels were manually categorised into three anatomical types: artery, bladder and other background tissues. It can be observed that the artery signal pixels are mainly located in the left of the scatter map, whereas the background tissue signal pixels distribute along a determined regression line $y = \beta x$. For conventional direct subtraction, the SI for a pixel *P* is obtained by subtracting its SI on DBIs from its SI on BBIs ($I_{Subtracted} = I_{Bright} - I_{Dark}$), which is proportional to the distance between the point *P* and the green line $y = x$ (line of unity) on the scatter plot (d_1). In many cases, the SIs of background tissues appear higher on BBIs than DBIs, which leads to residual background signal on subtracted angiograms, because there is still a considerable distance between the background pixel plot and the line of unity ($y = x$), particularly for background tissues with high SI such as the bladder.

An alternative method which could weight the subtraction to the actual distributions of background SIs would be expected to improve the suppression of background tissues ($I_{Subtracted} = I_{Bright} - \beta I_{Dark}$, no offset was added along the y-axis in all the models used in this study). Using such a method, a regression line (yellow line) for background pixels should be used, and the distance to the regression line would then be d_2 instead of d_1. Background tissue can thereby be reduced to close to zero, whereas the arterial signal would be less affected, as d_1 and d_2 of arterial pixels are very similar.

Figure 2 shows two examples of scatter plots (A and C) with normalised density (shown in the colour scale) and the corresponding maximum intensity projections (MIPs) of original raw images, directly subtracted angiograms and expected angiograms with improved background suppression (B and D). A and B are from thoracic 3D FSD (DANTE-balanced steady-state free precession (bSSFP)) (15,25), and B and D are from femoral 3D FBI. Reference angiograms with optimal background suppression and vascular visualisation were obtained by manual adjustment of the slope of the regression line to match the observed points on the scatter plot. Residual muscle signal (yellow arrowheads) can be observed on the direct subtracted thoracic FSD angiogram, while residual venous (yellow arrowheads) and testis signal (blue arrowheads) can be observed on direct subtracted femoral FBI angiograms.

The regression line can be obtained by different linear regression methods, but there are two key challenges to be addressed. The first challenge is the sensitivity to “outliers”. In some cases, such as thoracic MRA (Figure 2A & B), the presence of the heart leads to many flowing-blood pixels, which in the scatter plot lie in the region with high SI on BBIs and low SI on DBIs (the red dashed region on

Figure 2A). These points, which are considered as “outliers” in the linear regression, have large distances to the model prediction and thus would be given large weights in models like OLS or PCA (18). Therefore, the outliers would easily displace the regression line and generate an overlarge slope (the green line in Figure 2A), which can lead to excessive suppression and impair vascular signal. Secondly, the model may not be sensitive enough to pixels with high SI. In FBI (Figure 2C and D), muscle signal appears similar or even slightly lower (22,23) on BBIs than DBIs. Its corresponding pixels lie in the region with low SI on both BBIs and DBIs (the red dashed region on Figure 2C). In many cases such as femoral MRA, muscle is a much larger background component than other tissues and thus dominates the regression process, generating a relatively small regression coefficient (the green line on C) for OLS. Therefore, the background tissues with high SI on both BBIs and DBIs, such as the bladder and veins, are not fully suppressed.

Robust Regression

For OLS, the linear regression coefficient β can be solved by minimising the objective function which is given by

$$\beta_{OLS} = \arg\min_{\beta} \sum_{i=1}^{n} e_i^{\,2} \tag{1}$$

where n is the number of samples and e is the error of estimation $e_i = y_i - x_i\beta$.

The OLS model assumes a Gaussian distribution of errors e_i. However, in the presence of outliers, the long-tail error distribution may lead to a biased estimate of the regression coefficient. Robust regression methods have been proposed to down-weight the influence of outliers by modifying the objective function, accommodating more general error distributions and reducing the sensitivity to the magnitude of the residuals. The most common general method of robust regression is *M*-estimator (the name comes from the maximum-likelihood estimation), which attempts to minimise the sum of a chosen function $\rho(\cdot)$ of the residual errors (29). The function $\rho(\cdot)$ gives the contribution of each residual to the objective function.

Formally defined, *M*-estimators are given by

$$\beta = \arg\min_{\beta} \sum_{i=1}^{n} \rho\left(\frac{e_i}{\tau}\right) = \arg\min_{\beta} \sum_{i=1}^{n} \rho\left(\frac{y_i - x_i\beta}{\tau}\right) \tag{2}$$

where τ is a scale parameter determined empirically by the median absolute deviation (MAD) estimator: $\tau = \text{median}\left|e_i(\beta) - \text{median}\left(e_i(\beta)\right)\right| / 0.6745$. The constant 0.6745 makes the estimate unbiased for the normal distribution (30).

The function is minimised by setting the first partial derivatives of $\rho(\cdot)$ with respect to β to zero, resulting in a nonlinear equation

$$\sum_{i=1}^{n} x_i \psi\left(\frac{y_i - x_i\beta}{\tau}\right) = 0 \tag{3}$$

where $\psi(e) = \rho'(e)$ is called the influence function. The weight function is now defined as

$$w(e) = \begin{cases} \psi(e)/e, & \text{if } e \neq 0; \\ 1, & \text{if } e = 0. \end{cases} \tag{4}$$

Once the format of the weighted function is chosen, the equation can be solved using a numerical method called iteratively reweighted least squares (IRLS), which iteratively estimates the weighted least squares fit. The steps are as follows:

1. Use the least-squares estimate β_{OLS} from equation (1) as initial estimates $\beta^{(0)}$.
2. At each iteration *t*, calculate residuals $e_i^{(t-1)}$ and associated weights $w_i^{(t-1)} = w\left[e_i^{(t-1)}\right]$ from the previous iteration.
3. The new estimates of the regression coefficients are found using the matrix equation

$$\beta^{(t)} = \left[\mathbf{x}'\mathbf{W}^{(t\text{-}1)}\mathbf{x}\right]^{-1}\mathbf{x}'\mathbf{W}^{(t\text{-}1)}\mathbf{y} \tag{5}$$

where $\mathbf{x}$ is the model column vector, with x_i as its *i*-th element, and $\mathbf{W}^{t-1} = \text{diag}\left\{w_i^{t-1}\right\}$ is the current weight matrix.

Repeat steps 2 and 3 until the estimated coefficients satisfy the converge criterion:

$$\left|\beta^{(t)} - \beta^{(t-1)}\right| > \sqrt{\varepsilon}\max\left(\left|\beta^{(t)}\right|, \left|\beta^{(t-1)}\right|\right) \tag{6}$$

where ε is the floating-point relative accuracy corresponding to the distance from 1.0 to the next largest floating-point number (2^{-52} for double precision and 2^{-23} for single precision).

Weight Function

The selection of the weight function $w(\cdot)$ is the key to achieve robust regression for a specific problem. A typical function in *M*-estimation, the Welsch redescender (29) is used in this study, which is defined as:

$$\text{Welsch}(u) = \begin{cases} e^{-\left(\frac{u}{c}\right)^2} & \text{if } |u| < c \\ 0 & \text{if } |u| \geq c \end{cases} \tag{7}$$

$$c = 2.985$$

The tuning constant *c* gives coefficient estimates that have 95% asymptotic efficiency with respect to OLS at the Gaussian distribution (29). Further decreasing its value increases the downweight assigned to outlier points far from the regression line, and vice versa.

Figure 3 shows the weight maps of four weight functions investigated in this study. For OLS (or PCA), the weight function is $w = 1$. The weights are the same everywhere on the scatter map (Figure 3A), such as point *P* and *Q*. In this case, point *P* has a much larger influence on the regression result due to its longer distance to the current regression line.

For conventional robust regression (cRR) based on the Euclidean distance to the estimated regression line (Figure 3B), the weight function is given by $w(e) = \text{Welsch}(e)$, where $e = y - x\beta$. The points far from the regression line (point *P*) are given much smaller weights than the points closer to the line (point *Q*), which reduces the impact of the outliers corresponding to the arterial signal. However, cRR is not always effective at suppressing tissues with high SI on both BBIs and DBIs. For example, if the points of background tissues distribute along the line $y = \beta x$ $(\beta > 1)$ (red line), for points *R* and *S*, although both are located on $y = \beta x$, point *S* has a larger distance to the regression line. Therefore, point *S* would generate a heavier residual signal on the subtracted image and should ideally be given greater emphasis in the determination of β . However, cRR determines the weight based on Euclidean distance and gives point *S* a smaller weight, making the model less sensitive to the points with large SI values.

A potential improvement would be to use the polar coordinate system, determining weights from the polar angle instead of Cartesian distance. For robust regression based on deviation angle (RRDA), the weight function is given by $w(\theta) = \text{Welsch}(\theta)$, where θ is the deviation angle to the regression line given by $\theta = \arctan\left(\frac{y}{x}\right) - \arctan(\beta)$.

The contribution of high-SI points can still be too low due to their relatively small number in comparison with low-SI points corresponding to muscle and background air. Therefore, the normalised radial distance r can be used to further increase its sensitivity to points with large values:

$$w(\theta, r) = \text{Welsch}\left(\theta(\beta)\right) \cdot \left(\frac{r}{r_{\max}}\right)^{\alpha} \tag{8}$$

where $\theta(\beta) = \arctan\left(\frac{y}{x}\right) - \arctan(\beta)$ and $r = \sqrt{x^2 + y^2}$, α is a parameter controlling the influence of the normalised radial distance. It can be observed that point *S* has the same weight as *R* on Figure 3C and outweighs *R* on Figure 3D. This improved version of RRDA was used for the evaluation in this study.

Table 1 summarises the weight functions and characteristics of different regression methods mentioned above.

METHODS

Study Population and Imaging Protocols

Multiple datasets with differing NCE-MRA acquisition techniques were used in this study, including 36 coronal thoracic FSD-MRA datasets (DANTE-bSSFP)(15,25) from 16 healthy volunteers and 12 patients with central venous obstruction or restricted venous access; 13 coronal iliac FSD-MRA datasets (3 DANTE-bSSFP, 7 iMSDE-bSSFP (9,10), 3 iMSDE-FSE (31)) from 6 healthy volunteers; and 26 coronal femoral FBI-MRA (electrocardiographically-gated FSE) datasets from 17 healthy volunteers. The details of protocols are listed in Table 2.

All the images were acquired using 1.5 T MRI systems (Discovery MR450 or Optima MR450w; GE Healthcare, Waukesha, WI). Studies were approved by the local research ethics committee, and all participants gave informed consent.

Model Parameters

In this study, OLS, cRR and RRDA methods were evaluated on all the datasets. In RRDA, we adopted $\alpha=1$ for femoral FBI, which has a large number of muscle voxels with low SIs, and $\alpha=0.5$ for thoracic and iliac MRA images.

The 3D datasets in this study have a large number of voxels (8.4×10^6 –1.4×10^8), resulting in a large computational burden for real-time online processing. Therefore, a subset of voxels was randomly sampled for regression to increase computational efficiency. In a pilot study, we evaluated the performance of using different amounts of the randomly sampled data in all the datasets. The number of sampled voxels was increased from 2^{10} to 2^{23}, multiplying by 2 in each step, and the error between the results of partial data and full data was calculated. It was found that when the sampled voxels were larger than 2^{17} (131,072), the mean error in the regression coefficient due to this subsampling reduced to less than 0.01, which is visually undetectable on the intensity corrected angiograms. Therefore, the number of sampled voxels was fixed to 5×10^5 (500,000) for all datasets in this study. This corresponded to sampling ratios of 4.88%, 3.70% and 1.15%, and an estimated mean error of 0.0023, 0.0017 and 0.0017 in the regression line slope for thoracic FSD, iliac FSD and femoral FBI respectively. Compared with using full data, the use of partial data reduced the average computation times of thoracic FSD, iliac FSD and femoral FBI data from 20.2, 30.0 and 55.2 seconds to 0.6, 1.0 and 0.9 seconds respectively (4-Core 3.4 GHz CPU and 16 GB RAM).

Image Assessment

To evaluate the background SI difference between BBIs and DBIs, the SIs of specific background target tissues, such as muscle, liver, bladder, testis and veins (only on arteriograms) were measured on on the individual raw images before subtraction. Matched ROIs were drawn in representative regions of target tissues. One ROI was drawn on three selected slices for each dataset and for each background tissue. The slices were selected randomly but with the requirement of a large coverage of target tissues. The mean value of each background tissue was calculated for each dataset.

The calculated regression coefficients were compared with reference values determined by two trained observers with more than four years' experience in vascular MRI. Subjective manual determination of regression coefficients was performed based on both MIPs of subtracted images and scatter plots, using an interactive graphical interface developed in MATLAB (R2019a, Mathworks Inc., Natick, MA). Manually assessed optimal regression coefficients were determined by two observers independently based on the following method: the regression line was first positioned in the centre of the distribution of background signal voxels on the scatter plot and then adjusted to achieve optimal background signal suppression without impairing vascular signal on the MIP. The reference regression value was taken as the mean of the two manually determined optimal regression coefficients.

The results obtained by each regression model were compared with the reference values over different subjects using a paired, two-sided Student *t*-test. Pearson product-moment correlation analysis and Bland-Altman analysis were also used to evaluate the agreement between the results of each regression method and the reference values. A P-value <0.05 was considered statistically significant.

SI ratios of background tissue to vascular signal were also calculated for images obtained by direct subtraction and RRDA. SIs were measured from matched ROIs drawn in representative regions in the target tissues on the MIPs of subtracted images. For FBI-MR arteriography, two vascular ROIs were drawn in the lumen regions of arteries for each MIP; for FSD-MRA visualising both arteries and veins, one vascular ROI each was drawn from the lumen regions of arteries and veins respectively, and their mean value used as the vascular SI. Two ROIs were drawn for each type of background tissue, and the mean values were calculated for each dataset.

RESULTS

Figure 4 shows the signal levels of representative static tissues on DBIs and BBIs in the different study populations. SI differences can be observed in all these tissues, especially for organs containing plenty of water such as bladder and liver. The signal levels of most static tissues are significantly higher on BBIs than DBIs ($p<0.05$), leading to residual background signal on the subtracted angiograms. However, for femoral FBI, there is no significant difference between the muscle SI on BBIs and DBIs, which can bias the regression towards the distribution of other tissues such as bladder and veins.

Figure 5(A–E) shows an example result of thoracic FSD-MRA (DANTE-bSSFP) from a patient with central venous obstruction. The performance of RRDA is compared with OLS and direct subtraction. OLS (yellow solid line on E) was affected by outliers and overestimated the regression coefficient, leading to signal loss in small vessels (arrowheads on A to D). In contrast, both RRDA and cRR generated the correct regression line (red and green solid line on E) and thus suppressed residual muscle signal while preserving the blood signal (C and D). Similar results can be found in F–J showing an example of iliac iMSDE-FSE from a healthy volunteer.

An example of femoral FBI is shown in Figure 5 (K–O). The regression in cRR and OLS was dominated by the muscle voxels with a large number of voxels and low SI: their regression coefficients were insufficient to suppress veins (yellow arrowheads on L and M) or background tissues (blue arrowhead on L and M). RRDA was less sensitive to the muscle voxels (red solid line on J): background tissues such as testis (the blue arrowhead on N) and veins (yellow arrowheads in N) were suppressed, while the arterial signal is preserved. Note that some small vessels denoted by the green arrowheads on M are actually veins, which can be easily confused with arterial branches but can be suppressed by RRDA.

The statistical analysis results are listed in Table 3. Figure 6 shows the Bland-Altman plots and boxplots comparing the performance of different regression methods for different types of images. The iliac datasets using different sequences were categorised into one category due to their similar image characteristics and regression results.

OLS has high mean absolute errors and low correlation coefficients in all the three image types. In particular, due to its sensitivity to outliers, OLS tends to overestimate the regression coefficients in thoracic FSD, leading to a large bias of 0.293 and also large variation. cRR is more resistant to outliers. It has excellent performance in thoracic and iliac FSD. However, cRR has a bias of -0.089 in femoral FBI. The regression coefficients of cRR are smaller than the reference values in all the femoral FBI datasets evaluated in this study. RRDA achieved accurate and robust results in all the three types of images, with

small bias, small mean absolute error and high correlation coefficients. No significant differences were found between the RRDA results and reference values for any of the three methods.

A comparison of the tissue-to-vessel SI ratios between RRDA and direct subtraction is shown in Figure 7. In thoracic FSD, the muscle and liver-to-vessel SI ratios in RRDA reduced to 54.4% (from 0.18±0.08 to 0.10±0.05) and 93.0% (from 0.50±0.23 to 0.47±0.25) of their values in direct subtraction respectively; in iliac FSD, the muscle-, bladder- and testis- to-vessel SI ratios reduced to 63.1% (from 0.20±0.10 to 0.13±0.07), 76.5% (from 0.51±0.18 to 0.39±0.18) and 62.2% (from 0.35±0.20 to 0.22±0.15) respectively; in femoral FBI, the muscle-, bladder-, testis- and vein-to-artery SI ratios reduced to 36.0% (from 0.44±0.16 to 0.16±0.07), 35.2% (from 0.21±0.18 to 0.07±0.04), 45.1% (from 0.26±0.07 to 0.12±0.04) and 41.5% (from 0.20±0.08 to 0.08±0.06) respectively.

DISCUSSION

This study has developed a robust regression method to compensate for the SI differences of static background tissues between BBIs and DBIs in subtractive NCE-MRA. Signal level differences were found in almost all the static tissues for the subtractive NCE-MRA techniques investigated in this study. These differences lead to residual background signal when using direct subtraction, but this residual signal can be substantially reduced by using weighted subtraction, if an appropriate weighting factor is determined, corresponding to the regression coefficient between the background tissue signals.

FSD produces dark-blood images by using flow-sensitive preparation modules to suppress blood with fast flow. Although these modules are velocity-dependent, they can still impair the signal level of static residual background tissues. With MSDE or iMSDE, some static signal loss is inevitable, resulting from inherent T_2 decay, T_1 steady-state decay, diffusion (16), eddy currents from crusher gradients and imperfections in the 180° pulses. DANTE pulse trains cause a spoiling effect in flowing spins and suppress their signal. Static spins may form a steady state but still experience some signal decay, especially when eddy current effects distort the gradient waveforms and thus impair the phase preservation of the static signal (16).

FBI attenuates flowing spins due to the flow dephasing and flow void effect of the FSE sequence. Variable flip angles (32) or spoiling gradients (14) are normally employed to increase its sensitivity to blood flow velocity. Unfortunately, both of these approaches can also slightly reduce the signal from background tissues containing water or blood, such as veins, bladder and testis. The SI differences

between BBIs and DBIs can be more serious when the variable flip angles and flow-spoiled gradients are only employed in systolic acquisitions.

Another factor leading to the background SI difference is the varying TRs of systolic and diastolic acquisitions (21,22), which may be caused by two effects. First, the FBI sequence in this study uses an interleaved black/bright-blood acquisition, which alternates between bright- and dark-blood acquisitions in consecutive heartbeats. Since the diastolic acquisition has a longer trigger delay, *i.e.,* a longer period of T_1 recovery, background tissues would have slightly higher SI on the diastolic images than the systolic images. This is especially obvious for tissues with a long T_1 and T_2 such as the bladder, as their signals are not fully recovered within a TR of 2 or 3 R-R intervals and thus greatly fluctuate between BBIs and DBIs. In contrast, the original FBI technique (6,14) uses a sequential scheme that acquires consecutive slice encoding in bright- and dark-blood series to maintain the same TR and avoid this problem. Also, the FSD sequences used in this study acquire all images with the same cardiac trigger delay and do not have this issue. Another reason for varying TRs is the large R-R variations due to irregular heartbeats of subjects. This is more serious for the sequential acquisition used in the original FBI technique and the thoracic FSD sequence in this study. The influence of irregular heartbeats on background artefacts has been evaluated in volunteers with caffeine consumption or with cardiac arrhythmia by Kim *et al.* (21).

The sensitivity to outliers is the main limitation for using OLS. For a regression biased towards background tissues, vascular and heart voxels with different signal levels on BBIs and DBIs can be regarded as outliers and can affect the regression. cRR using IRLS can minimise the effect of outliers by assigning a weight to each data point according to its distance from the regression line. The results of our study show that cRR achieved accurate and robust results for thoracic and iliac FSD-MRA data. However, in femoral FBI, the muscle signal, which has similar low SI on BBIs and DBIs, has overwhelmingly the largest number of voxels and thus dominates the regression. To solve this problem, we adopted a polar system and deviation angle (in RRDA) instead of the Euclidean distance used in cRR. The reasons are as follows: Firstly, on the scatter plot, the SI difference between BBIs and DBIs is reflected as a deviation angle between the distribution of background points and the line $y=x$ (rotation), rather than a straight distance (translation). Secondly, compared with low SI tissues such as muscle, high SI tissues have higher residual SI on subtracted images and therefore should have a larger weight in order to achieve an optimal background suppression, but they are given smaller weights in cRR due to their longer distance to the regression line. A normalised radial distance with an exponential parameter α was added into the weighting function of RRDA to further increase its sensitivity to the points with large values. To achieve the optimal performance, the parameter α may need to be adjusted according to the voxel number of low SI background tissues.

Although background tissues were suppressed by using weighted subtraction, the desired vascular signals were only minimally affected. In this study, obvious vascular signal loss was only observed when the weighting factor is overestimated, for example, the OLS results in thoracic FSD-MRA. This is due to the distribution of vascular signal and background signal on the scatter plot and can be explained on Figure 1A. For the arterial pixels on Figure 1A, which locate on the bottom left of the scatter plot, their distance to the line $y = x$ (d_1) and the regression line (d_2) are very similar, while d_1 is much larger than d_2 for background pixels locating on the upper right. Therefore, using d_2 instead of d_1 does not change arterial SI much but can substantially reduce the SI of background tissues.

It should be noted that in conventional subtractive NCE-MRA techniques, background static signal suppression in unsubtracted raw images is still necessary. For example, STIR, magnetisation transfer contrast (33) and longer TE (32) have been used in FBI for background suppression in order to reduce the SI of background tissues and thereby any residual background SIs on subtracted angiograms. The weighted subtraction method developed in this study gives subtractive NCE-MRA techniques a larger tolerance of background SI difference between BBIs and DBIs. This potentially allows the imaging sequence design to maximise the arterial signal even at the cost of increasing background signals, *e.g.*, using minimum TE in FBI and selecting the flip angle maximising the arterial signal in bSSFP. Another potential sequence design is to generate images with maximum arterial signal but different background SIs on BBIs and DBIs, *e.g.*, using strong flow dephasing for the systolic acquisition and weak flow dephasing for the diastolic acquisition in FBI.

Another potential advantage of reducing the static background signal in angiograms is that it improves image sparsity, which we have recently shown can facilitate compressed sensing reconstruction and potentially improve reconstruction accuracy (34).

Although the regression results and background suppression effect of robust regression methods were analysed in volunteer and patient images, the diagnostic performance was not evaluated in this study. Future work will assess if clinical diagnosis or diagnostic confidence can be improved by background suppression using robust regression. Further work is also needed to evaluate the methods in other subtractive imaging sequences and anatomical regions.

CONCLUSION

In conclusion, robust regression approaches have been developed to correct the SI difference between background tissues on BBIs and DBIs for several subtractive NCE-MRA techniques, reducing residual

background signal on subtracted angiograms. Compared with OLS and the conventional robust regression method, RRDA proved more resistant to outliers across the range of different NCE-MRA methods investigated and more sensitive to background signal with high intensity. In this initial study, it achieved an accurate and robust performance applied to several different subtractive NCE-MRA techniques and different body regions.

ACKNOWLEDGEMENT

The authors acknowledge the financial support from the Addenbrooke's Charitable Trust and the National Institute for Health Research [Cambridge Biomedical Research Centre at the Cambridge University Hospitals NHS Foundation Trust]. The views expressed are those of the authors and not necessarily those of the NHS, the NIHR or the Department of Health and Social Care. Hao Li acknowledges the China Scholarship Council and Cambridge Trust for the fellowship support.

REFERENCE

1. Prince MR. Gadolinium-enhanced MR aortography. Radiology 1994;191:155–164 doi: 10.1148/radiology.191.1.8134563.

2. Ivancevic MK, Geerts L, Weadock WJ, Chenevert TL. Technical Principles of MR Angiography Methods. Magn. Reson. Imaging Clin. N. Am. 2009 doi: 10.1016/j.mric.2009.01.012.

3. Hartung MP, Grist TM, François CJ. Magnetic resonance angiography: current status and future directions. J. Cardiovasc. Magn. Reson. 2011;13:19 doi: 10.1186/1532-429X-13-19.

4. Kanda T, Ishii K, Kawaguchi H, Kitajima K, Takenaka D. High signal intensity in the dentate nucleus and globus pallidus on unenhanced T1-weighted MR images: relationship with increasing cumulative dose of a gadolinium-based contrast material. Radiology 2014;270:834–41 doi: 10.1148/radiol.13131669.

5. McDonald RJ, McDonald JS, Kallmes DF, et al. Intracranial Gadolinium Deposition after Contrast-enhanced MR Imaging. Radiology 2015;275:772–782 doi: 10.1148/radiol.15150025.

6. Miyazaki M, Lee VS. Nonenhanced MR Angiography. Radiology 2008;248:20–43 doi: 10.1148/radiol.2481071497.

7. Koktzoglou I, Lim RP, Oisin F, Edelman RR. Non-contrast Enhanced MRA. In: Syed MA, Raman S V., Simonetti OP, editors. Basic Principles of Cardiovascular MRI: Physics and Imaging Technique. Springer International Publishing; 2015. pp. 1–338. doi: 10.1007/978-3-319-22141-0.

8. Fan Z, Sheehan J, Bi X, Liu X, Carr J, Li D. 3D noncontrast MR angiography of the distal lower extremities using flow-sensitive dephasing (FSD)-prepared balanced SSFP. Magn. Reson. Med. 2009;62:1523–1532 doi: 10.1002/mrm.22142.

9. Priest AN, Graves MJ, Lomas DJ. Non-contrast-enhanced vascular magnetic resonance imaging using flow-dependent preparation with subtraction. Magn. Reson. Med. 2012;67:628–637 doi: 10.1002/mrm.23040.

10. Priest AN, Taviani V, Graves MJ, Lomas DJ. Improved artery-vein separation with acceleration-dependent preparation for non-contrast-enhanced magnetic resonance angiography. Magn. Reson. Med. 2014;72:699–706 doi: 10.1002/mrm.24981.

11. Li H, Priest AN, Patterson I, Graves MJ, Lomas DJ. Subtractive non-contrast-enhanced MRI of lower limb veins using multiple flow-dependent preparation strategies. Magn. Reson. Med. 2019;81:1769–1783 doi: 10.1002/mrm.27530.

12. Sheehan JJ, Fan Z, Davarpanah AH, et al. Nonenhanced MR Angiography of the Hand with Flow-Sensitive Dephasing–prepared Balanced SSFP Sequence: Initial Experience with Systemic Sclerosis. Radiology 2011;259:248–256 doi: 10.1148/radiol.10100851.

13. Miyazaki M, Sugiura S, Tateishi F, Wada H, Kassai Y, Abe H. Non-contrast-enhanced MR angiography using 3D ECG-synchronized half-Fourier fast spin echo. J. Magn. Reson. Imaging 2000;12:776–783.

14. Miyazaki M, Takai H, Sugiura S, Wada H, Kuwahara R, Urata J. Peripheral MR angiography: separation of arteries from veins with flow-spoiled gradient pulses in electrocardiography-triggered three-dimensional half-Fourier fast spin-echo imaging. Radiology 2003;227:890–896 doi: 10.1148/radiol.2273020227.

15. Priest AN, Mortensen KH, Lomas DJ. Comparison of DANTE- and iMSDE-based methods for subtractive NCE-MRA of the central thoracic vein. In: Proceedings of the 23rd Annual Meeting of ISMRM, Toronto, Canada. ; 2015. p. 2662.

16. Li L, Miller KL, Jezzard P. DANTE-prepared pulse trains: A novel approach to motion-sensitized and motion-suppressed quantitative magnetic resonance imaging. Magn. Reson. Med. 2012;68:1423–1438 doi: 10.1002/mrm.24142.

17. Wang J, Yarnykh VL, Yuan C. Enhanced image quality in black-blood MRI using the improved motion-sensitized driven-equilibrium (iMSDE) sequence. J. Magn. Reson. Imaging 2010;31:1256–63 doi: 10.1002/jmri.22149.

18. Li H, Wang S, Priest AN, Graves MJ, Lomas DJ. An optimised subtraction approach for subtractive NCE-MRA techniques based on principal component analysis. In: Proceedings of the Joint Annual Meeting ISMRM-ESMRMB, Pairs, France. ; 2018. p. 922.

19. Li H, Wang S, Priest AN, Graves MJ, Lomas DJ. Background tissue suppression for subtractive NCE-MRA techniques based on robust regression using the deviation angle. In: Proceedings of the 27th Annual Meeting of ISMRM, Montreal, Canada. ; 2019. p. 2094.

20. Lindley MD, Kim D, Morrell G, Heilbrun ME, Hanrahan CJ, Lee VS. Fat Saturation Improves Fresh Blood Imaging of Peripheral Vessels in the Calf Station. In: Proceedings of the 23rd Annual Meeting of ISMRM, Toronto, Canada. ; 2015. p. 4512.

21. Kim H, Park S, Kim EY, Park J. Retrospective multi-phase non-contrast-enhanced magnetic resonance angiography (ROMANCE MRA) for robust angiogram separation in the presence of cardiac

arrhythmia. Magn. Reson. Med. 2018;80:976–989 doi: 10.1002/mrm.27099.

22. Atanasova IP, Kim D, Storey P, Rosenkrantz AB, Lim RP, Lee VS. Sagittal fresh blood imaging with interleaved acquisition of systolic and diastolic data for improved robustness to motion. Magn. Reson. Med. 2013;69:321–328 doi: 10.1002/mrm.24576.

23. Storey P, Otazo R, Lim RP, et al. Exploiting sparsity to accelerate noncontrast MR angiography in the context of parallel imaging. Magn. Reson. Med. 2012;67:1391–1400 doi: 10.1002/mrm.23132.

24. Hoey ETD, Ganeshan A, Puni R, Henderson J, Crowe PM. Fresh blood imaging of the peripheral vasculature: An emerging unenhanced MR technique. Am. J. Roentgenol. 2010;195:1444–1448 doi: 10.2214/AJR.09.4184.

25. Priest AN, Low G, Graves MJ, Lomas DJ. Non-contrast-enhanced MR angiography of the thoracic central veins. In: Proceedings of the Joint Annual Meeting ISMRM-ESMRMB, Milan, Italy. ; 2014. p. 5597.

26. Foo TKF, Ho VB, Marcos HB, Hood MN, Choyke PL. MR angiography using steady-state free precession. Magn. Reson. Med. 2002;48:699–706 doi: 10.1002/mrm.10278.

27. Kimura T, Ikedo M, Takemoto S. Hybrid of opposite-contrast MR angiography (HOP-MRA) combining time-of-flight and flow-sensitive black-blood contrasts. Magn. Reson. Med. 2009;62:450–458 doi: 10.1002/mrm.22021.

28. Ye Y, Hu J, Wu D, Haacke EM. Noncontrast-enhanced magnetic resonance angiography and venography imaging with enhanced angiography. J. Magn. Reson. Imaging 2013;38:1539–1548 doi: 10.1002/jmri.24128.

29. Welsch RE. Robust regression using iteratively reweighted least-squares. Commun. Stat. - Theory Methods 1977;6:813–827 doi: 10.1080/03610927708827533.

30. Rousseeuw PJ, Croux C. Alternatives to the Median Absolute Deviation. J. Am. Stat. Assoc. 1993;88:1273–1283 doi: 10.1080/01621459.1993.10476408.

31. Priest AN, Murphy IG, Lomas DJ. Non-contrast-enhanced MRA using Velocity-sensitised , Acceleration-sensitised and Combined Sensitisation with Fast-Spin-Echo Readout. In: Proceedings of the 24th Annual Meeting of ISMRM, Singapore. ; 2016. p. 2554.

32. Storey P, Atanasova IP, Lim RP, et al. Tailoring the flow sensitivity of fast spin-echo sequences for noncontrast peripheral MR angiography. Magn. Reson. Med. 2010;64:1098–1108 doi:

10.1002/mrm.22510.

33. Morita S, Kojima S, Hirata M, et al. Unenhanced ECG-gated fast spin-echo MR digital subtraction angiography (MRDSA) using short echo-spacing three-dimensional sequence of femoral arteries: Initial experience. J. Magn. Reson. Imaging 2011;34:157–164 doi: 10.1002/jmri.22595.

34. Li H, Priest AN, Graves MJ, Lomas DJ. Highly Accelerated NCE-MRA Using Complex Subtraction with Intensity Correction: Improved Reconstruction Accuracy and Background Tissue Suppression. In: Proceedings of the 27th Annual Meeting of ISMRM, Montreal, Canada. ; 2019. p. 2067.

List of figure captions

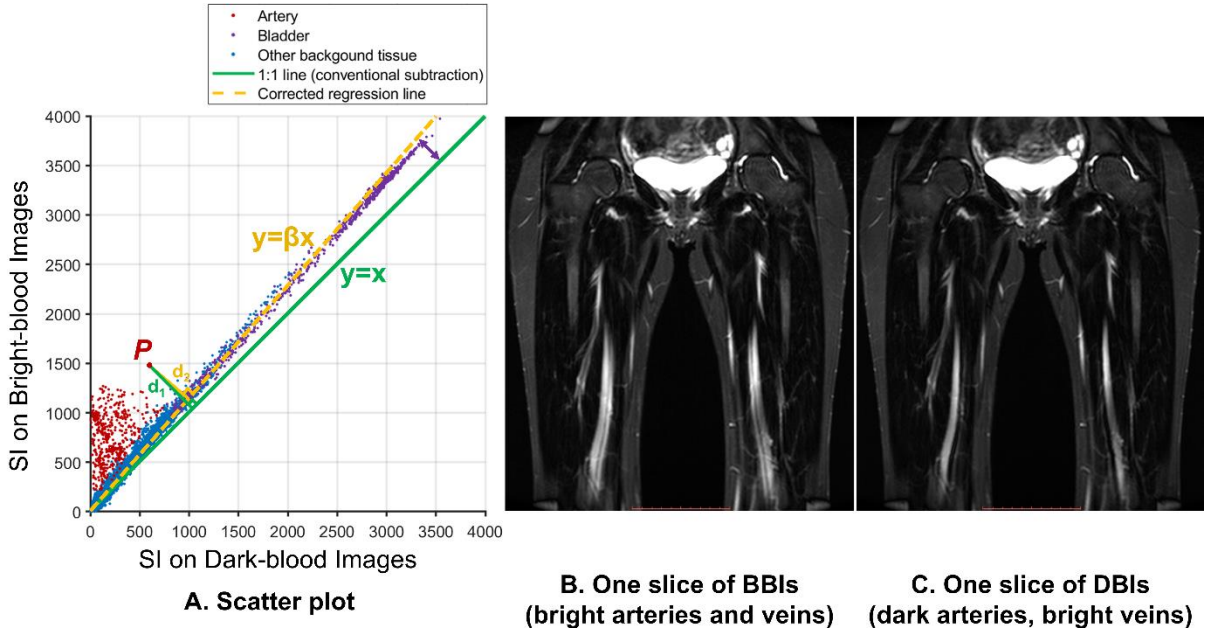

FIGURE 1 The scatter plot of the DBI and BBI SI for each pixel in one single slice (A) and the corresponding bright-artery (B) and dark-artery slice (C). The slice is selected from a femoral 3D FBI-MRA image set. The red points correspond to the artery signal, the purple points correspond to the bladder signal, and blue points correspond to other background tissues such as veins and muscles. Using conventional direct subtraction (green line), the SI of pixel *P* on the subtracted angiogram is proportional to d_1, while for the optimal subtraction (yellow line), the SI should be proportional to d_2.

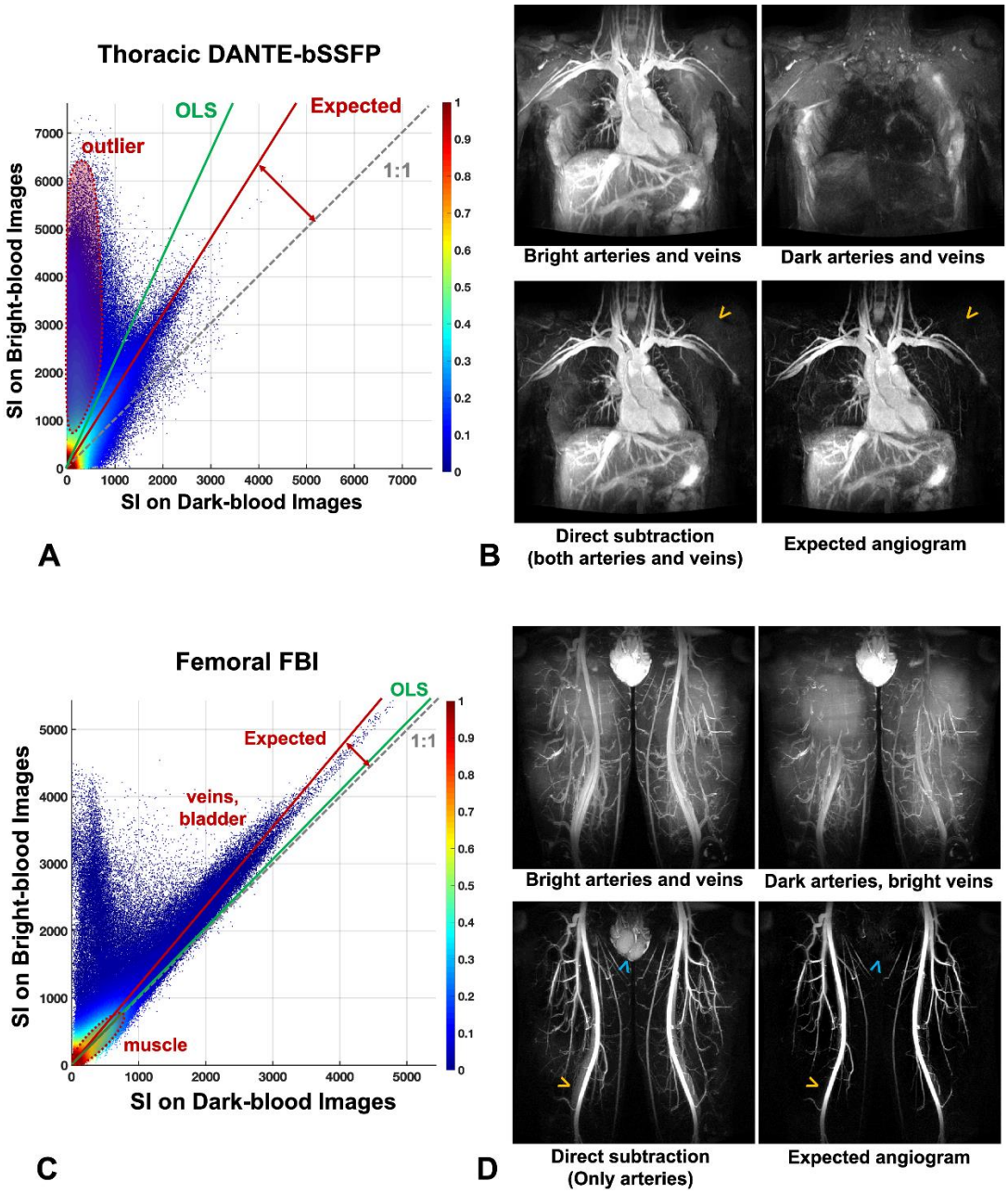

FIGURE 2. Two examples of thoracic 3D FSD (A and B, DANTE-bSSFP, intended to show both arteries and veins) and femoral 3D FBI (C and D, intended to show arteries only). A and C are scatter plots of the voxels from the whole 3D dataset. The coloured scale refers to the pixel number of each point divided by the maximum pixel number among all the pixels, which can be regarded as normalised density or frequency of the points. B and D are the corresponding MIPs of original raw images, directly subtracted angiograms and expected angiograms with improved background suppression. The green lines show the results of OLS, which fails to obtain the regression line of background voxels. The red lines are the expected results determined subjectively by manual selection.

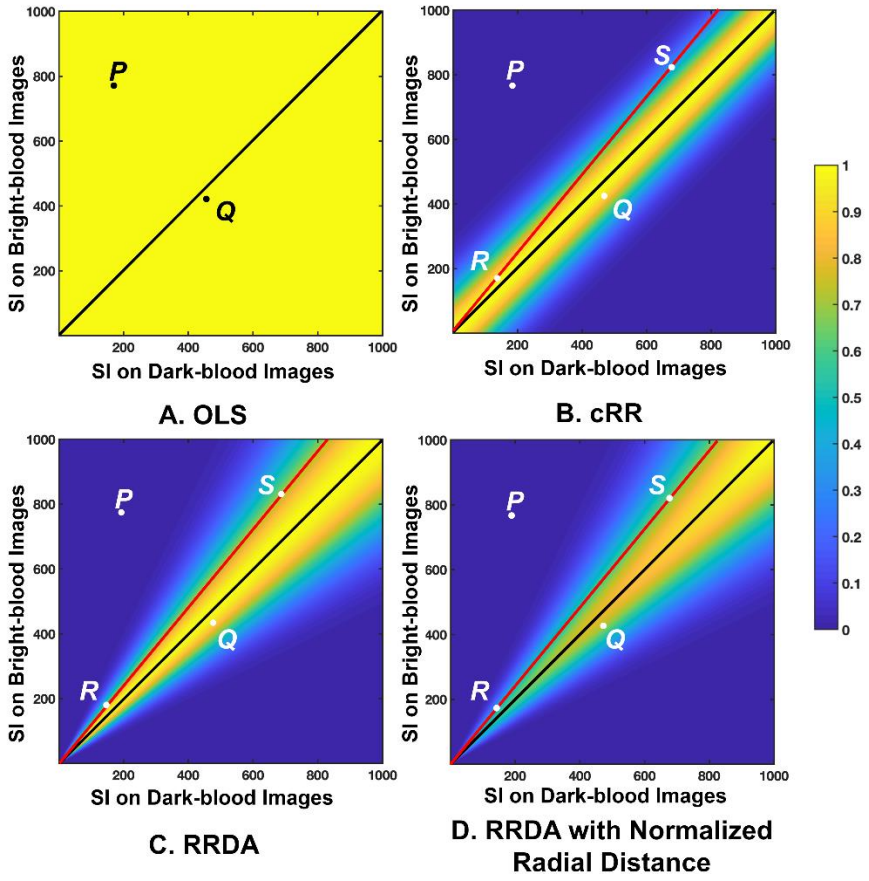

FIGURE 3. Weight maps of (A) OLS, (B) cRR, (C) RRDA and (D) improved RRDA (α=0.25) when the current regression line is $y=x$. All of the robust regression models down-weight points far from the model prediction. RRDA gives the points with large SI larger weights compared with cRR. Point *P* is an example point far from the current regression line, and point *Q* is a point close to the regression line. Points *R* and *S* both locate on the red line and have the same deviation angle, but point *S* has a larger distance to the current regression line. All of the robust regression models down-weight points far from the model prediction (point *P*). RRDA gives the points with large SI (point *S* in comparison with point *R*) larger weights compared with cRR.

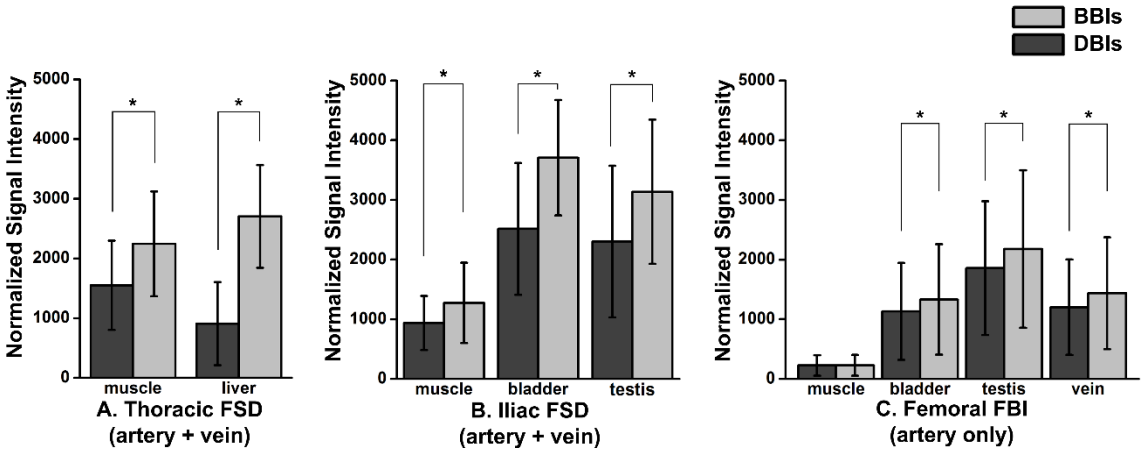

FIGURE 4. Signal levels of background tissues in BBIs and DBIs in thoracic FSD (A), iliac FSD (B) and femoral FBI (C). Asterisk (*) indicates significance at $P<0.05$ level. Signal levels are significantly lower on DBIs in all cases except for the muscle signal in femoral FBI.

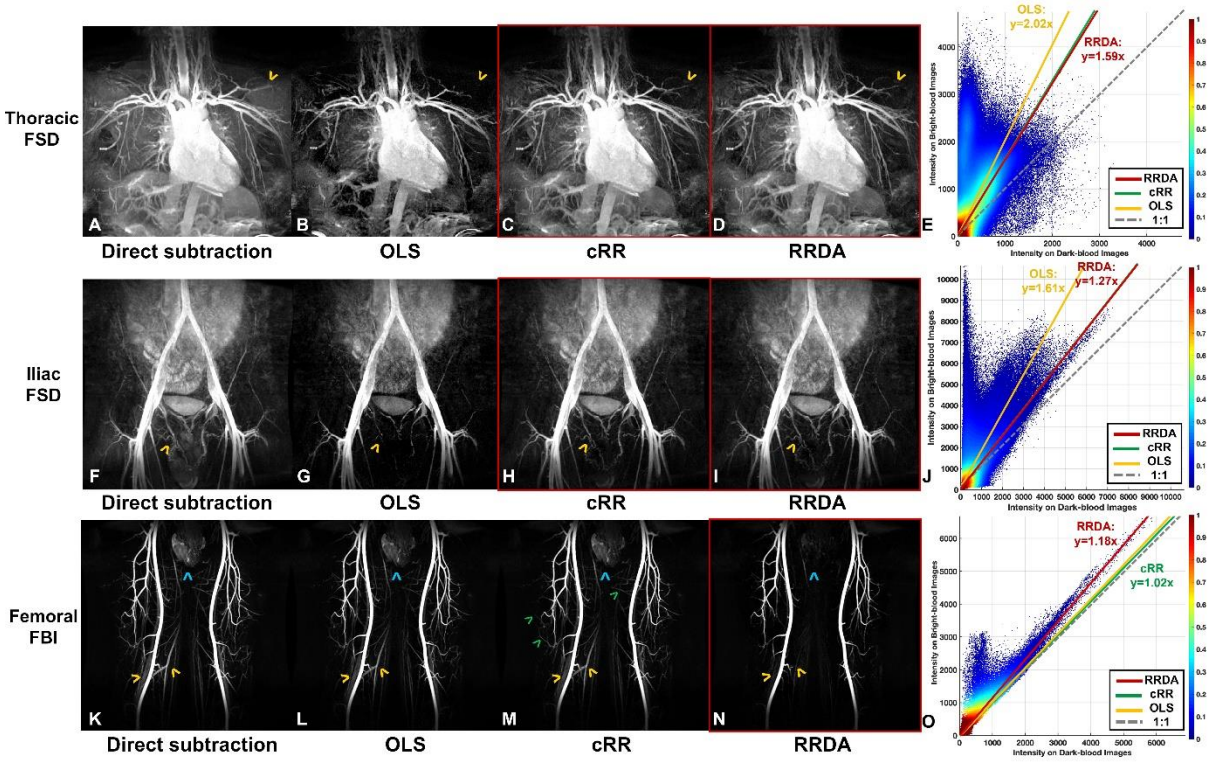

FIGURE 5. Example MIPs and the corresponding scatter plot of thoracic 3D DANTE-bSSFP (A–E), iliac 3D iMSDE-FSE (F–J) and femoral 3D FBI (K–O). E, J and O are scatter plots of the voxels from the whole 3D dataset with normalised density as the colour scale. The grey dashed lines on the scatter plots are the 1:1 line for the direct subtraction; the yellow, green and red solid lines are the regression lines estimated by OLS, cRR and RRDA respectively. The red boxes denote the regression results that agree most closely with the reference value. The arrowheads on MIPs denote the suppressed background tissue signal. The green arrowheads on M denote small venous branches which are easily confused with arterial branches but can be suppressed by RRDA. RRDA had good regression results in all the three cases. OLS generated an overlarge regression coefficient in thoracic and iliac FSD, which led to signal loss in small vessels. cRR failed to suppress the residual background signal in femoral FBI but agreed with RRDA in the other cases.

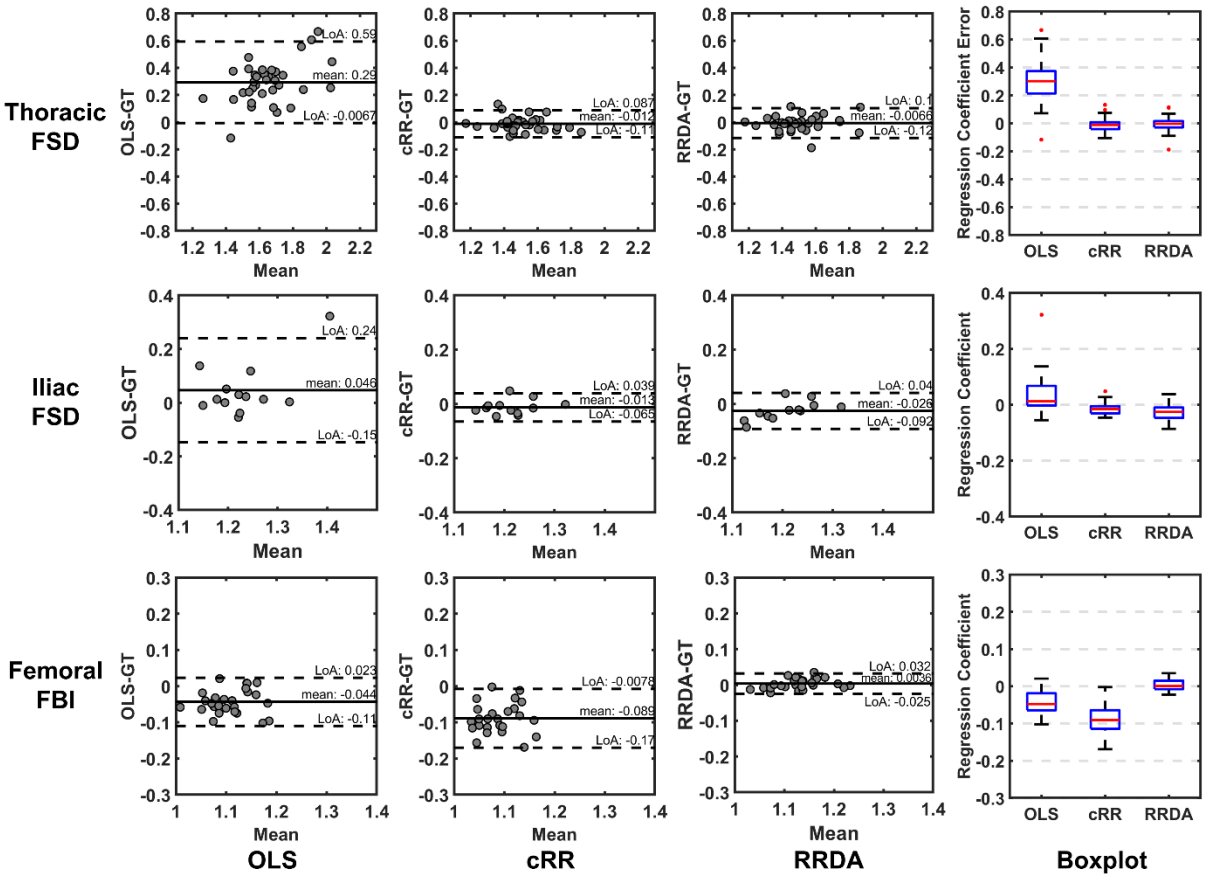

FIGURE 6. Bland-Altman plots and boxplots comparing the regression results of OLS, cRR and RRDA.

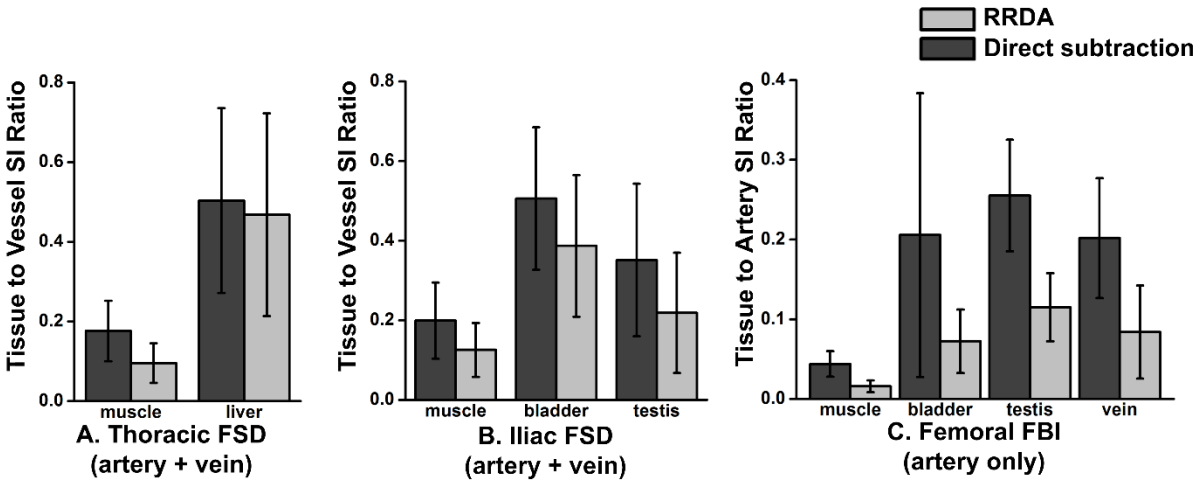

FIGURE 7. Comparison of the tissue-to-artery/vein SI ratios between RRDA and direct subtraction in thoracic FSD (A), iliac FSD (B) and femoral FBI (C). Statistically significant differences can be observed in all the cases (P<0.05).

List of table captions

TABLE 1. The weight functions and characteristics of different regression methods

Regression methods	Weight function	Robustness to outliers	Sensitivity to high-SI points
OLS/PCA	$w = 1$	Low	Medium
cRR	$w(e) = \text{Welsch}(e)$, where $e = y - x\beta$	High	Low
RRDA	$w(\theta) = \text{Welsch}(\theta)$ $\theta = \arctan\left(\frac{y}{x}\right) - \arctan(\beta)$	High	Medium
improved RRDA	$w(\theta, r) = \text{Welsch}(\theta(\beta)) \cdot r^{\alpha}$ where $\theta = \arctan\left(\frac{y}{x}\right) - \arctan(\beta)$ and $r = \frac{\sqrt{x^2 + y^2}}{r_{\max}}$	High	High

TABLE 2. Parameters Used for Thoracic FSD, Iliac FSD and Femoral FBI.

Area	Imaging target	Imaging sequence	Dataset number	Subject number, gender and age	Parameters
Thoracic	artery and vein	3D DANTE-bSSFP	36	16 volunteers (8 men and 8 women) and 12 patients (6 men and 6 women; age range 19–81 years)	Bright- and dark-blood acquisitions are sequential and had the same cardiac trigger delay and acquisition window. Free-breathing acquisitions using navigator gating (without slab-tracking, acceptance window 3–4 mm). Fat suppression: dual inversion-recovery (DIR) (25) with inversion times of approximately 250 ms and 20 ms. This aims to suppress fat but with reduced residual suppression of the blood signal by the short-time inversion recovery (STIR) pulse for short TR. Bright- and dark-blood acquisitions have the same cardiac trigger delay and acquisition window. DANTE: TR 1 ms, flip angle 10°, gradient 20 mT/m, echo train length (ETL) 150–270 pulses. bSSFP: acquisition matrix 256×256, acquisition slice number 32–56, slice thickness 4, FOV 400; R-R interval 2/3; flip angle 65°, TE/TR=1.0/2.7 ms, bandwidth ±125 kHz, acquisition window 115 ms. Each plane of *k*-space was acquired over two shots. Acquisitions accelerated by PI (array spatial sensitivity encoding technique, ASSET) with an acceleration factor of 3 in the phase-encoding direction.
Iliac	artery and vein	3D DANTE-bSSFP	3	6 volunteers (5 men and 1 women) and 2 patients (2 men, 52 years and 75 years old)	Bright- and dark-blood acquisitions were interleaved and had the same cardiac trigger delay and acquisition window. DANTE: TR 1 ms, flip angle 10°, gradient 20 mT/m, ETL 150–270 pulses; iMSDE: duration 4 ms, amplitude 6 mT/m, placed at the time of approximately peak venous flow within the cardiac cycle. Acquisition parameters for both bSSFP and FSE: acquisition matrix 256×256, acquisition slice number 44–72, slice thickness:2.4, FOV 340–380; R-R interval 2–3. Fat suppression: DIR. bSSFP: flip angle 65°, TE/TR=1.2/3.1 ms, bandwidth: ±125 kHz, acquisition window 198 ms. Each plane of *k*-space was acquired over two shots. ASSET factor 2. FSE: acquisition slice number 36–40, slice thickness 2.4 mm, FOV 340–360; TE_{eff} 62 ms, bandwidth ±83.3 kHz, ETL 64, echo spacing 3.1 ms, acquisition window 198 ms. Acquisitions accelerated by PI (Autocalibrating Reconstruction for Cartesian sampling, ARC) with an acceleration factor of 2 and half Fourier in the phase-encoding direction.
		3D iMSDE-bSSFP	7		
		3D iMSDE-FSE	3		
Femoral	artery	3D FBI	26	17 volunteers (11 men and 6 women; age range 24–45 years)	Systolic and diastolic acquisitions were interleaved, and their trigger delay times were 220ms and 500–1000ms respectively. Fat suppression: STIR with an inversion time of 174 ms. FSE: acquisition matrix 224×224–384×384, acquisition slice number 80, slice thickness 1.8–2 mm, FOV 400–440; TR=2–3 R-R intervals, TE_{eff} 30–60 ms, bandwidth ±62.5–83.3 kHz, ETL 60–80, echo spacing 3.6–4.6 ms, acquisition

					window 216–294 ms; accelerated by SPIRiT (32), PF and CS (overall acceleration factor 6–10, with a variable-density Poisson disk sampling pattern). Variable flip angles (33) (start from 105° and increase to 180° for the systolic acquisition; constant 180° for the diastolic acquisition) and flow-spoiled gradients (10% of one-half the area of the readout gradient for both systolic and diastolic acquisitions) (14) were both used to increase flow sensitivity.

TABLE 3. Comparison of Mean Regression Coefficients Calculated by Different Regression Methods versus the Reference Values.

Imaging Sequence	Statistics	OLS	cRR	RRDA	Reference values
Thoracic FSD	Mean coefficient	1.80±0.21	1.49±0.15	1.49±0.15	1.50±0.15
	Coefficient range	[1.35, 2.28]	[1.17,1.82]	[1.18.1.92]	[1.18,1.90]
	Bias	0.293±0.153	-0.012±0.051	-0.007±0.056	-
	P-value	<0.05	0.16	0.48	-
	Mean absolute error	0.293	0.039	0.038	-
	Pearson *r* value	0.69	0.94	0.93	-
	Number of datasets	36 datasets from 16 healthy volunteers and 12 patients			
Iliac FSD	Mean coefficient	1.25±0.10	1.20±0.07	1.18±0.08	1.21±0.06
	Coefficient range	[1.14,1.57]	[1.04,1.32]	[1.04,1.31]	[1.07,1.32]
	Bias	0.036±0.022	-0.013±0.027	-0.026±0.034	-
	P-value	0.12	0.10	0.05	-
	Mean absolute error	0.062	0.025	0.036	-
	Pearson *r* value	0.40	0.92	0.92	-
	Number of datasets	13 datasets from 6 healthy volunteers			
Femoral FBI	Mean coefficient	1.08±0.05	1.04±0.05	1.13±0.05	1.13±0.05
	Coefficient range	[1.03,1.23]	[0.95,1.12]	[0.98,1.16]	[1.04,1.23]
	Bias	-0.043±0.034	-0.089±0.041	0.004±0.014	-
	P-value	<0.05	<0.05	0.22	-
	Mean absolute error	0.047	0.089	0.012	-
	Pearson *r* value	0.75	0.62	0.96	-
	Number of datasets	26 datasets from 17 healthy volunteers			

Bias, *P*-values, mean absolute errors and Pearson *r* values are between automatic regression results and the reference values.